Journal of
Materials Chemistry C

Shear-aligned large-area organic semiconductor crystals through extended π- π interaction

Journal:	*Journal of Materials Chemistry C*
Manuscript ID	TC-ART-04-2023-001311.R1
Article Type:	Paper
Date Submitted by the Author:	24-May-2023
Complete List of Authors:	Zhang, Song; Stanford University, Chemical Engineering Talnack, Felix; TU Dresden, Center for Advancing Electronics Dresden Jousselin-Oba, Tanguy; Institut Lavoisier de Versailles Bhat, Vinayak; University of Kentucky College of Arts and Sciences, Wu, Yilei; Stanford University, Department of Chemical Engineering Lei, Yusheng; Stanford University, Chemical Engineering; Fudan University, Shanghai Frontiers Science Research Base of Intelligent Optoelectronics and Perception, Institute of Optoelectronics Tomo, Yoko; Stanford University, Chemical Engineering; Kyushu University, Department of Mechanical Engineering Gong, Huaxin; Stanford University, Chemical Engineering Michalek, Lukas; Stanford University, Chemical Engineering Zhong, Donglai; Stanford University, Chemical Engineering Wu, Can; Stanford University, Chemical Engineering Yassar, Abderrahim; Ecole polytechnique, LPICM, UMR 7647 CNRS Mannsfeld, Stefan; Technische Universität Dresden, Risko, Chad; University of Kentucky, Chemistry Frigoli, Michel; Université de Versailles Saint-Quentin en Yvelines UFR des Sciences, Institut Lavoisier de Versailles, CNRS Bao, Zhenan; Lucent Technologies, Bell Labs

ARTICLE

Shear-aligned large-area organic semiconductor crystals through extended π- π interaction

Received 00th January 20xx,
Accepted 00th January 20xx

DOI: 10.1039/x0xx00000x

Song Zhang,†[a] Felix Talnack,†[b] Tanguy Jousselin-Oba,[c] Vinayark Bhat,[d] Yilei Wu,[a] Yusheng Lei,[a,e] Yoko Tomo,[a,f] Huaxin Gong,[a] Lukas Michalek,[a] Donglai Zhong,[a] Can Wu,[a] Abderrahim Yassar,[g] Stefan Mannsfeld,*[b] Chad Risko,*[d] Michel Frigoli,*[c] and Zhenan Bao*[a]

Small molecule-based organic semiconductors are of broadly interest in organic field-effect transistors (OFETs) due to their potential for high crystallinity and electrical performance. The 2D molecule, TIPS-peri-pentacenopentacene (TIPS-PPP), which is the vertical extension of the 1D TIPS-pentacene (TIPS-PEN) molecule, offers a lower bandgap, higher aromaticity, and an enhanced π-π interaction with neighboring molecules in the solid state when compared to TIPS-PEN. However, an in-depth understanding of the relationship between the molecule structure, solid-state molecular packing, and the electronic properties has not been reported due to poor control over the TIPS-PPP crystallite size. In this work, we successfully engineered highly oriented large-area TIPS-PPP crystals through the solution shear coating technique. Compared with narrow ribbon-like TIPS-PEN crystals, TIPS-PPP crystals can grow centimeters long and over 500 µm wide. TIPS-PPP molecules are less susceptible to forming metastable polymorphs than TIPS-PEN molecules upon fast evaporation. The crystal structure of TIPS-PPP is also thermally stable at 250 °C. Notably, the anisotropic charge carrier mobility of TIPS-PPP crystals is resolved through fabricating bottom-gate top-contact devices, with a hole mobility of 3.1 $cm^2V^{-1}s^{-1}$ along the preferred packing direction. Further device optimization using top-gate bottom-contact devices improved the mobility up to 6.5 $cm^2V^{-1}s^{-1}$, which is among the highest for pentacene-derivative-based organic semiconductors.

1. Introduction

Organic electronic devices, including organic field effect transistors (OFETs), organic photovoltaics (OPVs), and organic light-emitting diodes (OLEDs), are of high academic and commercial interest.[1–10] As such, there remain substantial efforts to design new building blocks, i.e., π-conjugated small molecules and polymers, for organic semiconductors (OSCs) with improved electronical and optical performance. Due to their tunable crystalline packing motifs and band structures, small molecule OSCs play an essential role in understanding the interplay between crystal structure, thin film morphology, and charge transport. The crystal structures of pentacene (PEN) and its substituted derivatives like 6,13-bis(2-(tri-isopropylsilyl)ethynyl)pentacene (TIPS-PEN) are among the most investigated small molecules for OFETs, both through experiments and simulations.[11,12,21,22,13–20] Introducing the TIPS side chain to the pentacene core improves its solution solubility and stability, while a morphological transition occurred from herringbone packing to 2D lamellar π-π stacking.[22,23]

Recently, the synthesis of TIPS-peri-pentacenopentacene (TIPS-PPP) was reported by Frigoli and co-workers.[24] Compared with the TIPS-PEN structure with a 1D pentacene core, TIPS-PPP has two peri-fused pentacene cores, which leads to enhanced aromaticity and potentially more geometric overlap of neighboring π-conjugated backbones. Furthermore, TIPS-PPP exhibits a smaller band gap and 16 times higher stability than the TIPS-PEN in toluene.[24] Theoretical studies suggest that TIPS-PPP has a lower intramolecular reorganization energy and a larger intermolecular transfer integral compared to TIPS-PEN, with an estimated theoretical mobility one order of magnitude higher than TIPS-PEN.[24] However, only drop-casted TIPS-PPP thin films have been reported, which gave a modest charge carrier mobility of 0.3 cm^2/Vs for bottom-gate top-contact (BGTC) devices and 1 cm^2/Vs for top-gate bottom-contact (TGBC) devices, due to the limited size of the single crystalline domain. Thus, there remains a need for fabricating large-area TIPS-PPP thin film crystals to better understand the structure-electronic performance relationship and to further enhance the device characteristics.

Previously, our group utilized the solution shearing method to manipulate film processing conditions and subsequently control the morphology of TIPS-PEN.[15,16,25] Through the engineering of the kinetics of thin film drying and the crystal packing motif, we observed that a high charge carrier mobility can be achieved. This present work

---

[a] *Department of Chemical Engineering, Stanford University, Stanford, California, 94305, USA*
[b] *Center for Advancing Electronics Dresden (cfaed), Technische Universität Dresden, Dresden, 01062, Germany.*
[c] *Institut Lavoisier de Versailles, UMR CNRS 8180, University Paris-Saclay, 45 avenue des Etats-Unis, 78035 Versailles Cedex, France*
[d] *Department of Chemistry and Center for Applied Energy Research, University of Kentucky, Lexington, Kentucky 40506, USA*
[e] *Shanghai Frontiers Science Research Base of Intelligent Optoelectronics and Perception, Institute of Optoelectronics, Fudan University, Shanghai 200433, China*
[f] *Department of Mechanical Engineering, Kyushu University, 744 Mottoka Nishi-ku Fukuoka, 819-0395, Japan*
[g] *LPICM, UMR CNRS 7647, Ecole Polytechnique, 91128 Palaiseau Cedex, France*

† S.Z. and F.T. contribute equally to this work.

Electronic Supplementary Information (ESI) available: [details of any supplementary information available should be included here]. See DOI: 10.1039/x0xx00000x

utilized the solution shearing method to control the solvent evaporation and direct crystal growth of TIPS-PPP. Slow coating speeds resulted in aligned large-area crystalline domains for TIPS-PPP, while faster speeds favor the alignment of TIPS-PEN crystals. Further characterizations demonstrate that TIPS-PPP crystals exhibit preferential structural and thermal stability, as well as enhanced electronic performance, indicating the extension of π-backbone overlap as an effective strategy to improve the stability and performance of semiconductors.

2. Results and discussion

2.1 Solution shear coating

The chemical structures of TIPS-PPP and TIPS-PEN are shown in **Fig. 1a-b**. The PPP core consists of two rows of peri-fused pentacene. The same solubilizing TIPS side chain is introduced to the PPP core to ensure the same brick-wall motif packing as TIPS-PEN.[24] The solution shearing setup, comprising a top shearing blade and a bottom substrate on a hot stage, is depicted in **Fig. 1c**. During the shearing-blade movement, the solvent/substrate contact line moves along the shearing direction, leaving the semiconductor film deposited on the substrate. Fine-tuning the solvent evaporation, substrate wettability, and coating speed is essential to control the mass transport of solute and the crystallization process. Here, trichlorobenzene (TCB) was selected as the solvent due to the good solubility of TIPS-PPP up to 10 mg/ml. The strong intermolecular interaction between TIPS-PPP molecules led to a limited solubility (< 2 mg/ml) in solvents more commonly used for TIPS-PEN (i.e., toluene, mesitylene, and chlorobenzene). To avoid thin film dewetting, hydrophilic substrates like bare SiO$_2$/Si wafers or surface modified SiO$_2$/Si wafers are desired. However, hydroxyl groups on the substrate surface typically lead to charge trapping in pentacene-based electronic devices.[26,27]. As measured by photoelectron spectroscopy in atmosphere (PESA), TIPS-PPP crystals showed a much higher HOMO (Highest occupied molecular orbital) level ($-$5.04 eV) than that of TIPS-PEN ($-$5.30 eV) (**Fig. 1d**). A high off-current above 10^{-4} A was observed for OFET devices made of TIPS-PPP crystals on pristine SiO$_2$/Si substrates, which is an indication of charge trapping (Fig. S1, Supporting Information). To avoid charge trapping on the substrate, trichloro(phenethyl)silane (PTS) treatment was performed on SiO$_2$/Si wafers to passivate the hydroxyl group and passivate charge trapping sites.[28] The substrate temperature was maintained at 130 °C to allow a balanced TCB evaporation speed. It was found that 60% to 80% of the solvent boiling point (213 °C for TCB) is preferred to enable sufficient solute deposition without drying too quickly.[15,16,28]

The coating speed can greatly affect the mass transport, drying speed, and shear distortion force during the crystallization and growth rate of small-molecule crystals. To investigate the influence of the coating speed on the crystallite formation, a wide range of speeds, spanning from 0.02 mm/s to 0.5 mm/s were applied to deposit TIPS-PPP solution (8 mg/ml). Polarized optical microscope (POM) images of shear-coated TIPS-PPP thin films were shown in **Fig. 1e-i**. At a low coating speed below 0.06 mm/s, wide and long crystalline domains with widths above 500 µm and lengths over 1 cm could be achieved. It was noticed that these are twin crystals with a clear grain boundary parallel to the shearing direction, indicating highly oriented crystal growth. The inset shows periodic bright and dark patterns upon 13° rotation, indicating well-aligned molecular packing in individual crystalline domains. On the surface of green/yellow-colored crystalline domains, layers of blue/pink colored regions could be observed (**Fig. 1f**). These thicker regions could result from secondary crystallization (i.e., crystallization on existing crystals) at a later stage of solvent evaporation. Upon increased coating speed above 0.06 mm/s, the crystallite size was significantly reduced to sub-200 µm wide and 2 mm long strips (**Fig. 1g**).

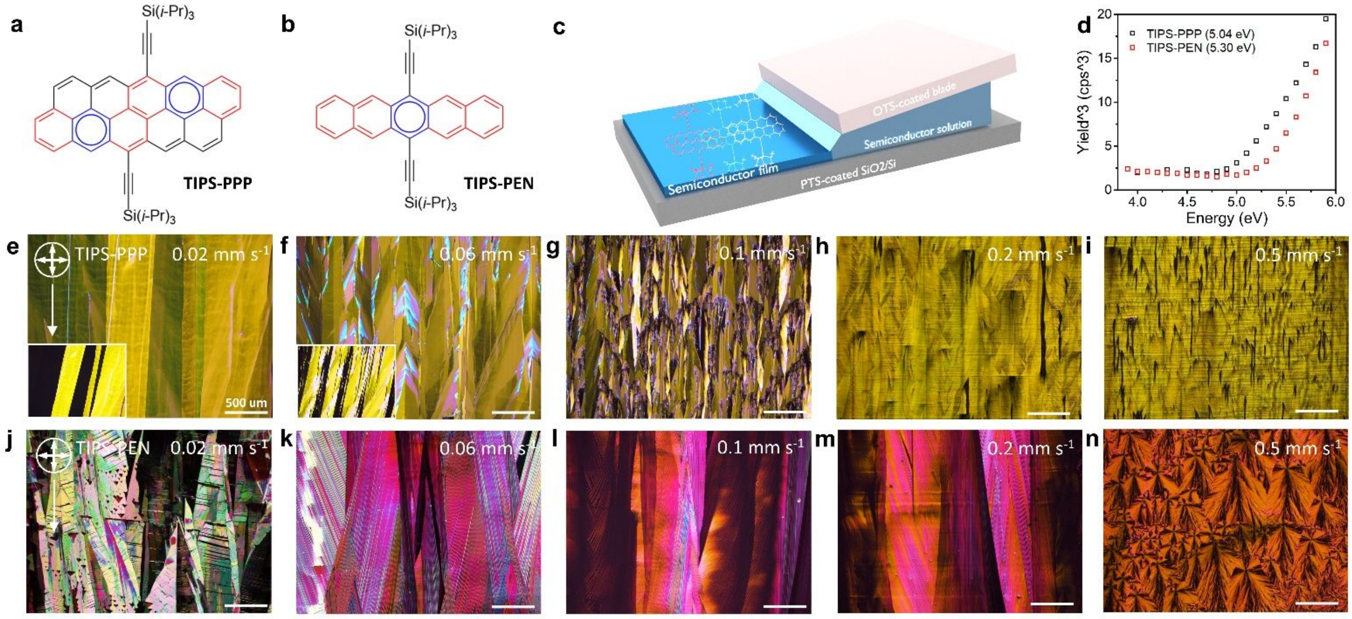

Fig. 1. Solution shear coating of TIPS-PPP and TIPS-PEN crystals. (a, b) Molecular structure of TIPS-PPP and TIPS-PEN. Reproduced with permission.[22] 2022, John Wiley and Sons. (c) 3D schematic of the solution shear coating process. (d) Photoelectron spectroscopy in air (PESA) plot showing the HOMO level of TIPS-PPP and TIPS-PEN. (e-n) Polarized optical microscope images of shear-coated (e-i) TIPS-PPP and (j-n) TIPS-PEN films under different coating speeds. The shearing direction is along the vertical direction. The inset represents rotated images at an angle of 13°.

Misoriented spherulites and small crystallites coexisted between these discontinuous crystallite strips. At 0.2 mm/s, the surface was fully covered by woven-like spherulites with curved grain boundaries, indicating a reduction in directionality (**Fig. 1h**). These spherulite domains further reduced in size upon increasing the coating speed to 0.5 mm/s (**Fig. 1i**). Additionally, the effect of the initial solution concentration on the film formation was studied by shear coating 3 mg/ml and 5 mg/ml TIPS-PPP solutions under the same conditions (Fig. S2, Supporting Information). The same trend as before was observed for these concentrations. However, the progression from oriented crystalline domains over strips to woven-like dendrites was shifted to lower speeds as the concentration decreased, i.e., the oriented crystalline strips occurred at a lower speed of 0.06 mm/s for 3 and 5mg/ml. These observations suggest that a longer crystallization time and sufficient mass transport are required for forming large, oriented TIPS-PPP crystals.

To understand the effect of molecular structure on crystal growth, TIPS-PEN crystals were fabricated through shear coating under the same conditions as TIPS-PPP (**Fig. 1j-n**). Under 0.02 mm/s, POM images showed multiple randomly oriented crystalline domains with large cracks inside (**Fig. 1j**). Upon slightly increasing the coating speed to 0.04 mm/s, previously observed as “fishbone-shaped” ribbon crystals appeared and exhibited near-unidirectional growth at an angle of ~ 25° to the shearing direction (**Fig. 1k**). These ribbon crystals were bundles of sub-10 um wide ribbons without clearly aligned grain boundaries and periodic patterns upon rotation under POM. Interestingly, these ribbon crystals were still accessible at a much faster speed of 0.2 mm/s, where more spherulites existed in TIPS-PPP films (**Fig. 1l-n**). This disparity in the sensitivity difference to coating speed results from different nucleation speeds and amounts of mass transport required for the crystal formation. To further understand this behavior, in-situ UV-vis absorption spectroscopy was utilized to monitor the π-π stacking peak (672 nm for TIPS-PEN and 830 nm for TIPS-PPP) during the free drying process of drop casted semiconductor solutions with the same concentration (Fig. S3, Supporting Information). The onset of π-π stacking peak formation for TIPS-PEN occurs 20 seconds earlier than that of TIPS-PPP, which was direct evidence that the intermolecular π-π stacking between individual 1D TIPS-PEN occurred faster than that the 2D counterpart core. Therefore, the extended 2D-core of TIPS-PPP produced wider and aligned crystalline domains given sufficient mass transport and incubation time.

2.2 Crystal structure

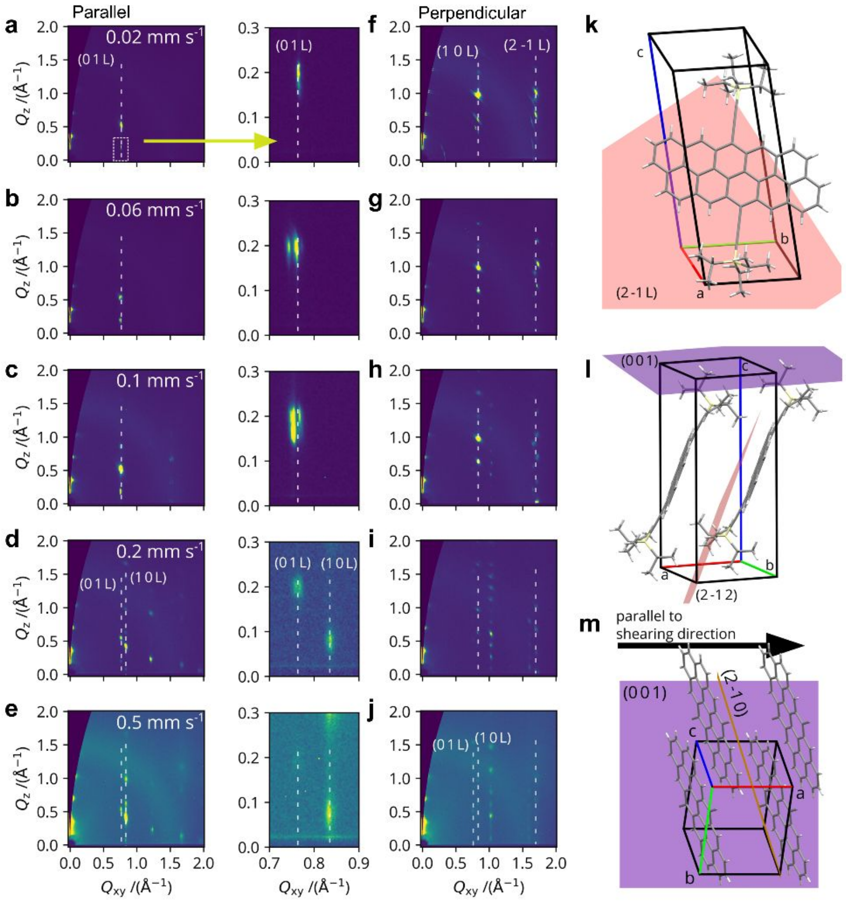

Fig. 2. Crystal structure analysis on shear-coated TIPS-PPP thin films. (a-j) 2D GIWAXS patterns of TIPS-PPP thin films under different coating speeds along the (a-e) parallel and (f-j) perpendicular direction. The (0 1 0) peak is plotted separately to better compare the peak location. (k-l) 3D schematics showing simulated TIPS-PPP molecules in a unit cell. The PPP core is parallel to the (2 -1 2) plane. The π- π stacking distance is calculated to be 3.67 Å. (m) 3D schematics showing the incident X-ray is parallel to the a-unit cell axis.

For shear-coated semiconductor films, the molecular packing and crystal alignment are deterministic parameters of their electrical performance. Here, grazing-incidence wide-angle X-ray scattering (GIWAXS) experiments were performed to obtain the 2D scattering patterns of TIPS-PPP thin films. The films were analyzed with the incident X-ray parallel and as well as perpendicular to the shearing direction (**Fig. 2a-j**), to assess the influence of the shear-coating on the orientation of the crystallites. To determine the crystal structure, a least-square-error optimization procedure was used to extract unit cell parameters based on the powder X-ray diffraction resulted from pristine materials and GIWAXS patterns (Table S1, Supporting Information).[24] The two unit cells were in good agreement, indicating a similar crystal structure in the thin film and the bulk. The indexed GIWAXS image is shown in the supplementary in Fig. S4, Supporting Information. To further show that both the bulk and thin film phases were almost identical, the observed GIWAXS image was compared to a calculated GIWAXS image in Fig. S5, Supporting Information. The similarity of the diffraction pattern showed that the crystal structures were alike.

The (0 0 L) peaks were observed in all images of **Fig. 2**, representing the vertical packing of TIPS-PPP molecules on the substrate with a lamellar distance of 1.73 nm. At below 0.06 mm/s, distinct crystallographic planes showed up along two directions, i.e., (0 1 L) peaks in the parallel direction and (1 0 L) peaks in the perpendicular direction (**Fig. 2a-c**). This observation indicated strong crystal alignment in the shear-coated films and agreed with the observed POM images. Such anisotropy was diminished upon an increase in coating speed at 0.1 mm/s, as evidenced by the appearance of (－1 1 L) peaks along the perpendicular direction (**Fig. 2h**). This feature marked the appearance of misoriented crystalline domains, such as spherulites and smaller crystallites in between crystalline stripes. A further increased coating speed resulted in randomly oriented spherulites and more peaks along both directions (**Fig. 2d,e,i,j**). From the crystal structure reported by Jousselin-Oba et al. the π-π stacking distance was estimated to be 3.334 Å and that the TIPS-PPP cores were orientated parallel to the (2 －1 2) plane (**Fig. 2k,l,m**).[24] From our GIWAXS measurements a slightly larger d-spacing of the (2 －1 2) plane of 3.37 Å was extracted (**Fig. 2f,g)**.

From the GIWAXS images of the highly orientated films obtained from slow shearing speeds, the orientation of the unit cell in respect to the shearing direction can be extracted. In the GIWAXS image shown in **Fig. 2a** with the X-ray beam parallel to the shearing direction only the (0 1 L) Bragg rod was visible, whereas for the perpendicular case shown in **Fig. 2f** only the (1 0 L) Bragg row was visible. This indicated that the a-unit cell axis was orientated parallel to the shearing direction (**Fig. 2m**). This contrasts with TIPS-PEN where the b-axis was orientated parallel to the shearing direction.[29]

In contrast to TIPS-PPP, TIPS-PEN thin films exhibited randomly distributed crystalline domains at a low coating speed, as evidenced by the (0 1 L) peaks along both parallel and perpendicular directions (**Fig. 3a,f**). From 0.06 mm/s to 0.2 mm/s, (0 1 L) peaks shown in the parallel direction slowly disappeared, indicating an increased degree of alignment for TIPS-PEN ribbons (**Fig. 3b-d**). At 0.5 mm/s, more orientations showed up with multiple diffraction patterns at the same position along both directions (**Fig. 3e,j**). Previous work on solution shearing of TIPS-PEN molecules in toluene demonstrated that a higher coating speed leads to faster crystallization and solvent evaporation, resulting in kinetically trapped metastable polymorphs.[16] These polymorphs displayed a more oblique molecular packing under increased coating speed, resulting in shorter π-π stacking distance, shorter (1 0 1) d-spacing, and longer (0 1 0) d-spacing. In this study, similar lattice strain-induced molecular displacement behavior was noticed. With increased coating speed from 0.02 mm/s to 0.5 mm/s, the (0 1 0) peak shifted to a lower q_{xy}, thus increasing d-spacing from 7.44 Å to 7.67 Å (**Fig. 3f-j**). This trend agreed with the previous report, where the d-spacing increased from 7.83 Å to 8.13 Å.[16] However, these changes were not seen in shear-coated TIPS-PPP thin films with a relatively undisturbed (0 1 0) packing distance (**Fig. 2a-e**). TIPS-PEN was known to have multiple polymorphs depending on the processing condition and temperature.[15] The observation here suggested TIPS-PPP displayed only one packing structure accessible during shear coating. This could potentially be attributed to the presence of a more extended π-structure, resulting in a stronger interaction between adjacent TIPS-PPP molecules.

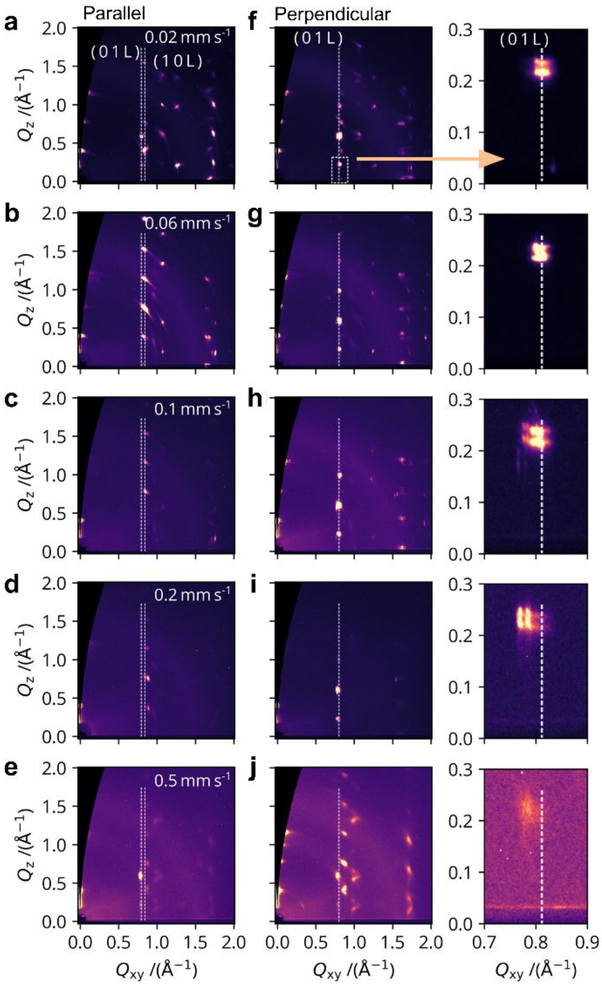

Fig. 3. 2D GIWAXS patterns of TIPS-PEN thin films under different coating speeds along the (a-e) parallel and (f-j) perpendicular directions. To better compare the peak location, the (0 1 0) peak is plotted separately.

2.3 Thermal stability

In addition to the structural stability, the thermal stability of TIPS-PPP and TIPS-PEN crystals were also compared. It is known that TIPS-PEN crystals go through thermally induced phase transformations, as shown by two endothermic transitions from 120-130 °C and 160-170 °C in the differential scanning calorimetry (DSC) curve (**Fig. 4a**).[30,31] These transitions resulted from the onset of conformational freedom for TIPS side chains, leading to changes in unit cell geometry. As a result, crystallographic cracks were widely distributed in TIPS-PEN crystals coated under 130 °C, as shown in Fig. 1j. At first glance, no noticeable cracking behavior was observed in the POM image of aligned TIPS-PEN ribbon crystals (**Fig. 4b)**. However, a zoom-in atomic force microscopy (AFM) image captured the existence of sub-micrometer-long and nanometer-wide cracks across the crystal surface (**Fig. 4c**). Notably, the crack growth direction can provide rich information about the molecular packing of TIPS-PEN molecules.[30] Due to the weaker interaction between the edges of pentacene core compared with the intermolecular interaction between pentacene cores, primary cracks typically formed along the crystal long axis, and secondary cracks propagated between pentacene cores during thermal expansion and extraction (**Fig. 4d**).

Unlike TIPS-PEN, TIPS-PPP did not exhibit thermal transitions up to 300 °C in the DSC curve, indicating no observable structural changes in unit cells (**Fig. 4e**). To further examine the potential cracking behavior, POM images were taken for TIPS-PPP crystals on a hot stage under nitrogen protection (**Fig. 4i**). Here, two regions with clear grain boundaries were selected on the film surface. While no cracking behavior was seen in region 1 (~ 100 nm) up to 250 °C, region 2 with a higher film thickness (> 200 nm) showed symmetric cracks growing outwards the grain boundary direction at 80° under 250 °C (**Fig. 4f-g, 4j-k**). Importantly, the molecular orientation did not change, as evidenced by the periodic patterns in rotated POM images and unchanged GIWAXS patterns (Fig. S6, Supporting Information). AFM images were taken using an as-cast sample to investigate the origin of the cracking behavior. No apparent features were observed from region 1 except a height change (~10 nm) across the grain boundary (**Fig. 4h**). In contrast, an extra layer of crystal (~ 4 nm) along the grain boundary appeared in region 2, which could result from secondary crystallization (**Fig. 4l**). Meanwhile, clear boundaries between neighboring crystals propagating from the twin grain boundary at an angle of 100° with respect to the shearing direction can be identified. Notably, the cracks are orientated in angle of 100° with the shearing direction as well. In combination from the previous described GIWAXS results, this shows that the a-axis of the TIPS-PPP unit cell is orientated parallel to the shearing direction.

2.4 OFET Characteristics

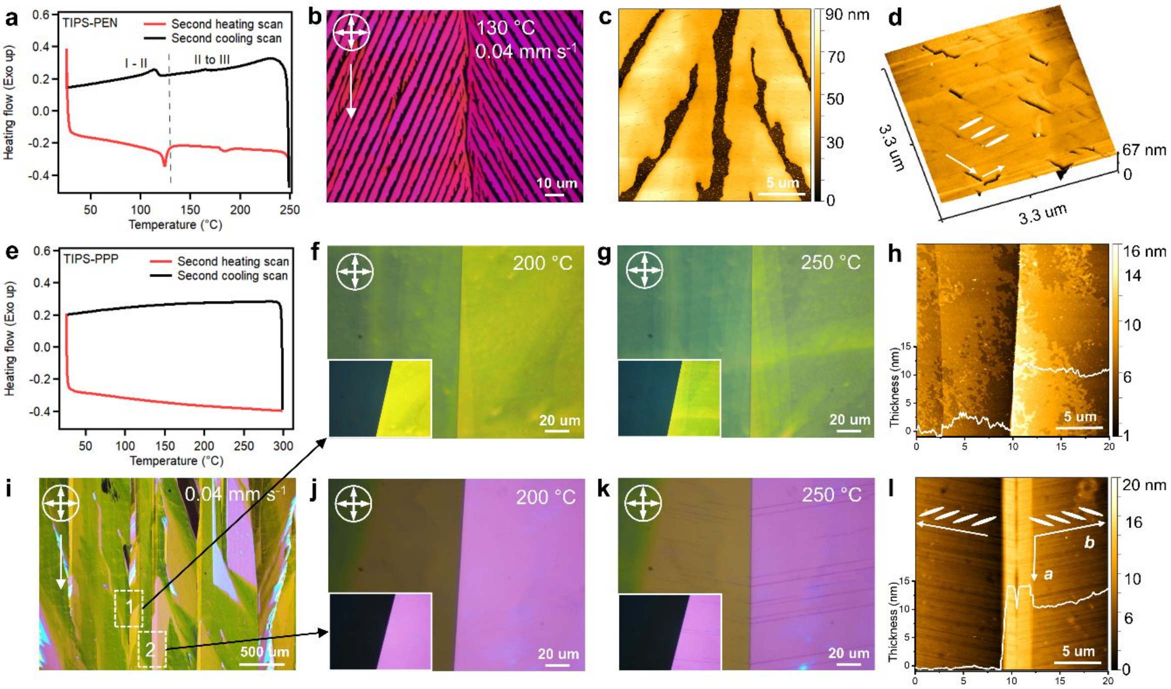

Fig. 4. Thermal-stability comparison between (a-d) TIPS-PEN and (e-l) TIPS-PPP. (a,e) DSC curves showing the second heating and cooling scan of (a) TIPS-PEN and (e) TIPS-PPP, respectively. (b, i) POM image of shear coated (b) TIPS-PEN and (i) TIPS-PPP crystals at a speed of 0.04 mm/s under 130 °C. (c,d) AFM image of TIPS-PEN ribbon crystals showing the cracking behavior. (f, g, j, k) POM images of (f, g) region 1 and (j, k) region 2 under different temperatures. Region 2 shows a green/yellow color, and region 2 shows a blue/red color with a higher film thickness. (h, l) AFM image of as-cast TIPS-PPP crystals in two regions.

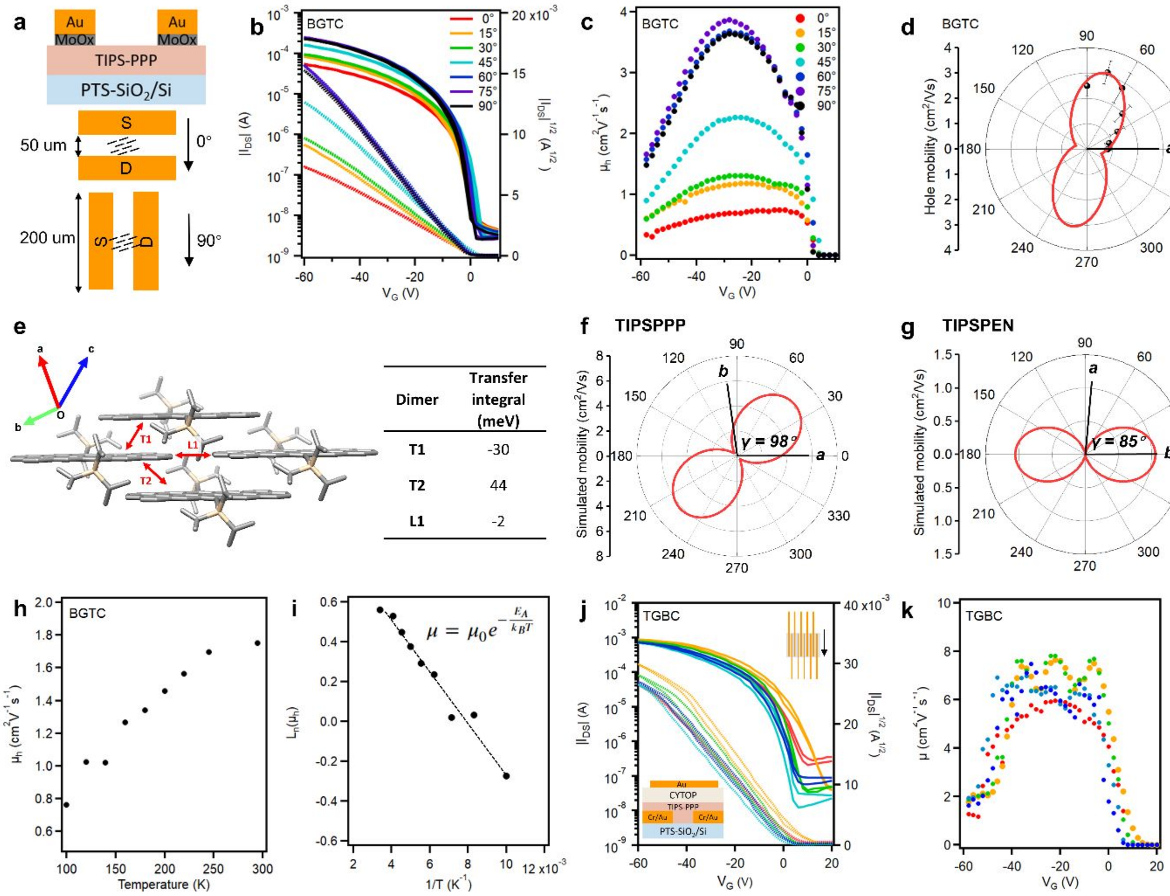

Fig. 5. Experimental and simulated OFET performance. (a) 2D schematic showing the BGTC device geometry and the electrode orientation. The arrow represents shearing direction and the angle between shearing direction and charge transport direction ranges from 0 to 90 degrees. (b) Representative transfer curves and (c) extracted mobility against gate voltage for BGTC devices under different orientations. (d) Polar plot of experimental mobility for TIPS-PPP crystal. The a-unit cell axis is parallel to the shearing direction. Sample number n=6. (e) DFT simulation of HOMO-HOMO coupling between neighboring TIPS-PPP molecules. (f, g) Polar plots of simulated mobility for (f) TIPS-PPP and (g) TIPS-PEN projected on the a-b plane of the unit cell. (h, i) Temperature dependence of experimental mobility using one BGTC device. (j) Representative transfer curves and (k) extracted mobility against gate voltage for TGBC devices. Five representative devices are shown in different colors. The shearing direction is perpendicular to the charge transport direction.

Owing to the large and aligned crystalline domains in TIPS-PPP thin films, it is feasible to deposit multiple devices on the same crystal to study the crystal orientation effect on the charge carrier mobility. Here, bottom-gate top-contact (BGTC) devices were fabricated using small electrodes with a channel length of 50 um and width of 200 um. The channel direction was kept at an angle to the shearing direction, from 0° (parallel) to 90° (perpendicular) in 15° steps (**Fig. 5a**, Fig. S7, Supporting Information). MoO$_3$ was deposited as a hole extraction layer between TIPS-PPP and the gold electrode. All devices were operated in the saturation regime and under ambient conditions, with a source/drain voltage of − 60 V and a gate voltage ranging from 20 to − 60 V. The representative output curve can be found in Fig. S8, Supporting Information. **Fig. 5b** showed representative transfer curves for each angle, where the drain current increased from 0° to 75°, then slightly dropped at 90°. All curves showed limited hysteresis with a high on-off current ratio of around 10^5, suggesting limited trap states at the semiconductor/dielectric interface.[32] Meanwhile, a strong linearity in the $|I_{SD}|^{1/2}$ (V_G) graph was observed, with a reliability factor ranging from 104% to 110%. However, non-ideal humps were noticed in the gate voltage-dependent mobility curves for devices with a high mobility, indicating the dominance of contact resistance under a high gate voltage **(Fig. 5c)**.[33] **Fig. 5d** plotted the extracted charge carrier mobility at different angles, where a high mobility was observed at an angle from 60° to 90° with an averaged mobility of 3.13 ± 0.47 cm^{2}V^{-1}s^{-1} at around 75°. This mobility was ten times higher than that of drop-casted TIPS-PPP thin films and twice of shear-coated TIPS-PEN crystals with a high reliability factor.[24,34–36]

To understand the observed orientation-dependent mobility, density functional theory (DFT) calculations were performed to determine the coupling on four adjacent TIPS-PPP molecules. The dimers T1 and T2 showed comparative HOMO-HOMO coupling of 44 and 30 meV **(Fig. 5e)**. The chromophore had a hole reorganization energy of 90 meV, slightly less than that of pentacene (95 meV) and TIPS-PEN (92 meV), all computed at the same level of theory. Simulated charge carrier mobilities reveal that the prominent charge carrier transport direction was around 15° off the perpendicular to the backbone direction. Further, the simulated maximum mobility of TIPS-PEN crystals is six-time smaller than TIPS-PPP (1.25 cm^{2}V^{-1}s^{-1} versus 7 cm^{2}V^{-1}s^{-1}) with less balanced charge transfer characteristics, as evidenced by a larger-tilted polar plot and more anisotropic transfer integral (Fig. S9, Supporting Information).[37] For comparison with experimental mobility, a polar plot was used to depict the angle-dependent simulated mobility within the a/b plane of the unit cell (**Fig. 5f**). An overall agreement with the experimental mobility was observed with a 25° angle difference for TIPS-PPP crystals (Fig. 5d). This difference could be due to slight differences in the packing of the shear-coated crystal and the fact that molecular motions were not considered in the simulation. For TIPSPEN, the maximum mobility has been observed along the b-unit cell axis, which was parallel to the shearing direction (**Fig. 5g**).[29,38]

The temperature dependence of charge carrier transport was also investigated under high vacuum from 300 K to 100 K. Instead of band-like transport, a thermally activated charge transport was observed, where the hole mobility continuously decreased with reduced temperature **(Fig. 5h)**. Similar behavior had been observed for bar-coated TIPS-PEN crystals and attributed to the exponentially increased contact resistance as temperature decreased.[34] Next, the mobility was plotted against the inverse of temperature to extract the activation energy using an Arrhenius-like equation. An activation energy, E_A, of 10.9 meV was calculated for TIPS-PPP crystals, which was much lower than shear-coated TIPS-PEN crystals (15 meV) or spin-coated TIPS-PEN spherulites (>20 meV) **(Fig. 5i)**.[34,39,40] Thus, the trapping states in these TIPS-PPP devices were much shallower than that of TIPS-PEN-based OFET devices. Followed by the temperature dependence, the grain boundary effect was explored by fabricating OFET devices with a longer channel width of 1000 um. On highly aligned crystals with clear grain boundaries, the mobility showed a negligible difference with and without one single grain boundary in the channel (Fig. S9, Supplementary Information). However, for thin films coated under 1 mm/s with significantly reduced crystallite size, the mobility dropped over one order of magnitude with notably increased threshold voltage (Fig. S10, Supporting Information). Such a trend agreed with previous works showing a greater number of grain boundaries leading to a high density of traps that can drastically reduce the mobility.[41]

In addition to BGTC devices, different device geometries and dielectrics were also studied to improve the charge carrier mobility of TIPS-PPP crystals. Bottom-gate bottom-contact (BGBC) devices and top-gate bottom-contact (TGBC) devices were fabricated using the same semiconductor layer. Cr/Au electrodes were first deposited on PTS-coated SiO_2/Si wafers with a channel dimension of 2000 um (width) by 50 um (length). Then, the TIPS-PPP solution was shear-coated perpendicular to the charge transport direction to obtain the BGBC device (Fig. S11, Supporting Information). On top of the BGBC devices, a layer of Cytop dielectric was applied, followed by gold deposition to fabricate TGBC devices (**Fig. 5j**). While both devices showed limited hysteresis in the transfer curve, a relatively high threshold voltage below 10V was noticed, which could result from injection issues between TIPS-PPP and Au electrodes.[42] Similar to the BGTC devices, a non-linear mobility-voltage relationship showed up at a high gate voltage due to contact resistance, which could also be seen from the output curve (**Fig. 5k**, Fig. S11, Supporting Information). BGBC and TGBC devices showed an average saturated mobility of 0.86 ± 0.11 $cm^2V^{-1}s^{-1}$ and 6.47 ± 0.86 $cm^2V^{-1}s^{-1}$, respectively, with a reliability factor from 103% to 120%. The mobility in the linear region also agreed with the saturated region despite the contact resistance effect (Fig. S11, Supporting Information). The much-improved performance of TIPS-PPP on the Cytop dielectric could be attributed to its trap-free characteristics, high hydrophobicity, and low dielectric constant.[43–45] Overall, the hole mobility of TIPS-PPP crystals in this work is among the highest for solution-coated pentacene-based semiconductors.[29,36,43,46–48] The extension of π- π overlapping provides an exciting pathway for the future engineering of high-performance organic semiconductors.

3. Conclusions

This work investigates the effects of 1D and 2D pentacene-like molecules on the morphology, thermal, and electronic properties of resulting OSC. The solution shearing technique is employed to fabricate large-area aligned crystals by carefully monitoring the shearing speed and crystal growth. Compared to needle-like TIPS-PEN (1D) crystals, TIPS-PPP (2D) crystals span centimeters long and over 500 µm wide. Owing to strong π-π interactions, these crystals retain stable molecular packing under shearing and show thermal resistance up to 250°C. DFT simulations suggest that TIPS-PPP has larger intermolecular transfer integrals and a lower reorganization energy than TIPS-PEN. Consequently, TIPS-PPP crystals exhibit significantly improved charge carrier mobility compared to TIPS-PEN crystals. The synthesis and study of other 2D semiconductor materials is ongoing.

4. Experimental

4.1 Solution shear coating

A solution of ~15 µl of TIPS-PPP in 1,2,4-trichlorobenzene (3 to 8 mg/ml) was heated overnight at 120°C on a hot plate. The solution was then applied between an octadecyltrichlorosilane (OTS)-treated shearing blade and a phenyltrichlorosilane (PTS)-treated SiO_2/Si substrate. A tilt angle of 8° with a 10 µm gap size was kept for the top blade, while the substrate temperature was maintained at 130°C. Detailed descriptions of the solution shear coating setup and the OTS/PTS treatment on SiO2-Si substrate have been reported previously.[16,49]

4.2 Crystal characterization

POM images were taken using Nikon ECLIPSE LV100 microscope. In-situ annealing experiments were performed using an Instec HCS 3 hot plate with an INSTEC mK1000 temperature controller. UV/Vis/NIR absorption spectra were recorded using a Cary 6000i spectrophotometer. PL spectra were acquired using HORIBA Fluorolog3 spectrofluorometer equipped with a picosecond TCSPC module. Photoelectron spectroscopy in air (PESA) measurements were taken on a Riken AC-2 photoelectron spectrometer with a power setting of 100 nW and a power number of 0.33. The sample for PESA was prepared by solution shear coating on a PTS-modified glass slide. DSC is collected with TA Q2500 instrument at a heating/cooling rate of 10 °C min^{-1}.

4.3 Morphological characterization

GIWAXS experiments were performed at beamline 11-3 of the Stanford Synchrotron Radiation Lightsource. An incident X-ray with a photon energy of 12.7 keV was used at an angle of 0.12°. Samples were stored in a helium chamber to avoid air scattering and oxidation upon heating. A two-dimensional detector (MAR-225) was used to collect data at a sample-to-detector distance of 300 mm. The data was processed using the WaveMetrics Igor Pro with a Nika script, WAXStools software and WxDiff. AFM images were collected using tapping mode on a Bruker Icon AFM with NSC15/Al-BS (MikroMasch, Tallinn, Estonia) AFM cantilever (typical resonant frequency of 325 kHz and force constant of 40 N·m^{-1}). Images were recorded with 512 pixels and a scan-rate of 0.8 Hz. The data was evaluated and depicted with Gwyddion SPM software.

4.4 OFET device fabrication

The BGTC devices were fabricated by patterning a shadow mask on top of blade-coated thin films, followed by thermally evaporating 3 nm molybdenum oxide and 60 nm gold with an evaporation rate of 0.1 Å s $^{-1}$ and 0.4 Å s $^{-1}$, respectively. The electrode for BGBC/TGBC devices was fabricated by evaporating 3 nm chromium and 40 nm gold on top of the SiO_2/Si wafer with a channel length of 50 µm and channel width of 2000 µm. For TGBC devices, a layer of ~1 um thick Cytop dielectric was directly spin-coated on top of the semiconductor, followed by thermal evaporating 40 nm gold as the gate. The geometrical capacitance of the CYTOP layers was measured to be ~2.1 nF cm^{-2}. All devices were measured under ambient environment using a Keithley 4200 semiconductor parameter analyzer.

4.5 Density functional theory (DFT) calculations

All DFT calculations were performed with Gaussian16.[50] The intermolecular electronic couplings were computed using the fragment molecular orbital approach (FMO-DFT) at the PBE/6-31G(d,p) level of theory.[51–53] The input geometries for the dimer were obtained from the crystal structure. An electronic coupling calculator from the OCELOT API was used to compute the charge transfer integrals.[54] The inner-sphere reorganization energy was evaluated with the four-point model.[55] To reduce computing time, the trialkyl silicon chains were removed, and calculations were only performed for the most extensive π-conjugated system. The neutral, cation and anion geometry were optimized with IP-tuned LC-ωHPBE/Def2SVP with normal mode analysis to confirm minima on the potential energy surface.[56–58] The formalism proposed by Goddard et al. to estimate anisotropy in charge carrier mobility.[59] We compute the hopping rate W using the Marcus-Hush equation[60] $W = \frac{V^2}{\hbar}\sqrt{\frac{\pi}{\lambda k_B T}} exp\left(-\frac{\lambda}{4k_B T}\right) \#(1)$ where V is the electronic coupling, λ is the reorganization energy, T is the temperature set to 298 K and k_B is the Boltzmann constant. The angular dependence of mobility is computed using the following equation -

$$\mu_\phi = \frac{e}{2k_B T}\sum_i W_i r_i^2 P_i cos^2\gamma_i cos^2(\theta_i - \phi)\#(2)$$

$$P_i = \frac{W_i}{\sum_i W_i}\#(3)$$

where i represents a specific hopping path with a hopping distance of r_i, hopping rate W_i, hopping probability P_i. $(\theta_i - \phi)$ is the angle between the conducting channel and the hopping path, ϕ is the orientation of the conducting channel relative to the reference axis and γ_i is the angle between the hopping paths and the reference plane which is set to 0.

Author Contributions

The project was conceived by Z.B. and M.F.. S.Z. conducted the experiments involving solution coating, POM, GIWAXS, AFM, in-situ UV-vis, and OFET device fabrication. F.T. and S.M. conducted the crystal structural analysis. T. J-O., A.Y., and M.F. synthesized the TIPS-PPP molecule. V.B. and C.R. conducted the DFT simulation. Y.W. conducted the PL and PESA experiment. Y.L. helped with crystal analysis. Y.T. conducted the temperature dependent OFET measurement. H.G. performed DSC measurements. L.M., D.Z., and C.W. provided helpful discussions. All authors contributed to the editing of the manuscript.

Conflicts of interest

There are no conflicts to declare.

Acknowledgements

F.T. and S.M. acknowledge financial support from the German Research Foundation (DFG, MA 3342/6-1), the German Excellence Initiative via EXC 1056 “Center for Advancing Electronics Dresden” (CFAED) and the TU Dresden Graduate Academy. M.F. and A.Y. acknowledge financial support from the Agence Nationale de la Recherche ANR-16-CE07-0024 (GATE). V.B. and C.R. at the University of Kentucky acknowledge funding by the National Science Foundation through award number DMR 1627428. Supercomputing resources were provided by the University of Kentucky Information Technology Department and Center for Computational Sciences (CCS). L.M. acknowledges funding through the Walter Benjamin Fellowship Program by the Deutsche Forschungsgemeinschaft (DFG 456522816). Y.W. acknowledges financial support from the Office of Naval Research (award N00014-19-1-2453). Part of this work was performed at the Stanford Nano Shared Facilities (SNSF), supported by the National Science Foundation under award ECCS-2026822. Use of the Stanford Synchrotron Radiation Lightsource, SLAC National Accelerator Laboratory, is supported by the U.S. Department of Energy, Office of Science, Office of Basic Energy Sciences under Contract No. DE-AC02-76SF00515.

Notes and references

1 O. Inganäs, *Adv. Mater.*, 2018, **30**, 1800388.
2 J. Wang, Z. Zheng, Y. Zu, Y. Wang, X. Liu, S. Zhang, M. Zhang and J. Hou, *Adv. Mater.*, 2021, **33**, 2102787.
3 P. Cheng and Y. Yang, *Acc. Chem. Res.*, 2020, **53**, 1218–1228.
4 S. Song, H. Hou, J. Wang, P. Rao and Y. Zhang, *J. Mater. Chem. A*, 2021, **9**, 3931–3939.

5 H. Sirringhaus, *Adv. Mater.*, 2014, **26**, 1319–1335.

6 H. Bronstein, C. B. Nielsen, B. C. Schroeder and I. McCulloch, *Nat. Rev. Chem.*, 2020, **4**, 66–77.

7 Y. Li, X. Huang, H. K. M. Sheriff and S. R. Forrest, *Nat. Rev. Mater.*, 2022, **8**, 186–201.

8 Y. Jiang, Z. Zhang, Y.-X. Wang, D. Li, C.-T. Coen, E. Hwaun, G. Chen, H.-C. Wu, D. Zhong, S. Niu, W. Wang, A. Saberi, J.-C. Lai, Y. Wu, Y. Wang, A. A. Trotsyuk, K. Y. Loh, C.-C. Shih, W. Xu, K. Liang, K. Zhang, Y. Bai, G. Gurusankar, W. Hu, W. Jia, Z. Cheng, R. H. Dauskardt, G. C. Gurtner, J. B. H. Tok, K. Deisseroth, I. Soltesz and Z. Bao, *Science.*, 2022, **375**, 1411–1417.

9 S. Wang, J. Xu, W. Wang, G. J. N. Wang, R. Rastak, F. Molina-Lopez, J. W. Chung, S. Niu, V. R. Feig, J. Lopez, T. Lei, S. K. Kwon, Y. Kim, A. M. Foudeh, A. Ehrlich, A. Gasperini, Y. Yun, B. Murmann, J. B. H. Tok and Z. Bao, *Nature*, 2018, **555**, 83–88.

10 Z. Zhang, W. Wang, Y. Jiang, Y.-X. Wang, Y. Wu, J.-C. Lai, S. Niu, C. Xu, C.-C. Shih, C. Wang, H. Yan, L. Galuska, N. Prine, H.-C. Wu, D. Zhong, G. Chen, N. Matsuhisa, Y. Zheng, Z. Yu, Y. Wang, R. Dauskardt, X. Gu, J. B. H. Tok and Z. Bao, *Nature*, 2022, **603**, 624–630.

11 J. E. Anthony, J. S. Brooks, D. L. Eaton and S. R. Parkin, *J. Am. Chem. Soc.*, 2001, **123**, 9482–9483.

12 J. E. Anthony, D. L. Eaton and S. R. Parkin, *Org. Lett.*, 2002, **4**, 15–18.

13 J. E. Anthony, *Angew. Chemie - Int. Ed.*, 2008, **47**, 452–483.

14 S. M. Ryno, C. Risko and J. L. Brédas, *J. Am. Chem. Soc.*, 2014, **136**, 6421–6427.

15 Y. Diao, K. M. Lenn, W. Y. Lee, M. A. Blood-Forsythe, J. Xu, Y. Mao, Y. Kim, J. A. Reinspach, S. Park, A. Aspuru-Guzik, G. Xue, P. Clancy, Z. Bao and S. C. B. Mannsfeld, *J. Am. Chem. Soc.*, 2014, **136**, 17046–17057.

16 G. Giri, E. Verploegen, S. C. B. Mannsfeld, S. Atahan-Evrenk, D. H. Kim, S. Y. Lee, H. A. Becerril, A. Aspuru-Guzik, M. F. Toney and Z. Bao, *Nature*, 2011, **480**, 504–508.

17 S. C. B. Mannsfeld, M. L. Tang and Z. Bao, *Adv. Mater.*, 2011, **23**, 127–131.

18 F. Molina-Lopez, H. Yan, X. Gu, Y. Kim, M. F. Toney and Z. Bao, *Adv. Funct. Mater.*, 2017, **27**, 1605503.

19 T. Sakanoue and H. Sirringhaus, *Nat. Mater.*, 2010, **9**, 736–740.

20 R. B. Campbell, J. M. Robertson and J. Trotter, *Acta Crystallogr.*, 1961, **14**, 705–711.

21 F.-J. Meyer zu Heringdorf, M. C. Reuter and R. M. Tromp, *Nature*, 2001, **412**, 517–520.

22 A. Maliakal, K. Raghavachari, H. Katz, E. Chandross and T. Siegrist, *Chem. Mater.*, 2004, **16**, 4980–4986.

23 C. Wang, H. Dong, W. Hu, Y. Liu and D. Zhu, *Chem. Rev.*, 2012, **112**, 2208–2267.

24 T. Jousselin-Oba, M. Mamada, K. Wright, J. Marrot, C. Adachi, A. Yassar and M. Frigoli, *Angew. Chemie Int. Ed.*, 2022, **61**, e202112794.

25 Y. Diao, B. C. K. Tee, G. Giri, J. Xu, D. H. Kim, H. A. Becerril, R. M. Stoltenberg, T. H. Lee, G. Xue, S. C. B. Mannsfeld and Z. Bao, *Nat. Mater.*, 2013, **12**, 665–671.

26 Z. T. Zhu, J. T. Mason, R. Dieckmann and G. G. Malliaras, *Appl. Phys. Lett.*, 2002, **81**, 4643–4645.

27 C. Pannemann, T. Diekmann and U. Hilleringmann, *J. Mater. Res.*, 2004, **19**, 1999–2002.

28 Y. Diao, B. C. K. Tee, G. Giri, J. Xu, D. H. Kim, H. A. Becerril, R. M. Stoltenberg, T. H. Lee, G. Xue, S. C. B. Mannsfeld and Z. Bao, *Nat. Mater.*, 2013, **12**, 665–671.

29 C. Teixeira da Rocha, K. Haase, Y. Zheng, M. Löffler, M. Hambsch and S. C. B. Mannsfeld, *Adv. Electron. Mater.*, 2018, **4**, 1800141.

30 J. Chen, J. Anthony and D. C. Martin, *J. Phys. Chem. B*, 2006, **110**, 16397–16403.

31 J. Chen, C. K. Tee, J. Yang, C. Shaw, M. Shtein, J. Anthony and D. C. Martin, *J. Polym. Sci. Part B Polym. Phys.*, 2006, **44**, 3631–3641.

32 H. F. Haneef, A. M. Zeidell and O. D. Jurchescu, *J. Mater. Chem. C*, 2020, **8**, 759–787.

33 J. W. Borchert, R. T. Weitz, S. Ludwigs and H. Klauk, *Adv. Mater.*, 2022, **34**, 2104075.

34 M. Berteau-Rainville, A. Tamayo, T. Leydecker, A. Pezeshki, I. Salzmann, M. Mas-Torrent and E. Orgiu, *Appl. Phys. Lett.*, 2021, **119**, 103301.

35 S. Wang, X. Zhao, Y. Tong, Q. Tang and Y. Liu, *Adv. Mater. Interfaces*, 2020, **7**, 1901950.

36 K. Kim, K. Nam, X. Li, D. Y. Lee and S. H. Kim, *ACS Appl. Mater. Interfaces*, 2019, **11**, 42403–42411.

37 F. Steiner, C. Poelking, D. Niedzialek, D. Andrienko and J. Nelson, *Phys. Chem. Chem. Phys.*, 2017, **19**, 10854–10862.

38 O. Ostroverkhova, D. G. Cooke, F. A. Hegmann, R. R. Tykwinski, S. R. Parkin and J. E. Anthony, *Appl. Phys. Lett.*, 2006, **89**, 192113.

39 A. Y. B. Meneau, Y. Olivier, T. Backlund, M. James, D. W. Breiby, J. W. Andreasen and H. Sirringhaus, *Adv. Funct. Mater.*, 2016, **26**, 2326–2333.

40 A. Laudari and S. Guha, *Phys. Rev. Appl.*, 2016, **6**, 044007.

41 S. Wo, R. L. Headrick and J. E. Anthony, *J. Appl. Phys.*, 2012, **111**, 073716.

42 M. Waldrip, O. D. Jurchescu, D. J. Gundlach and E. G. Bittle, *Adv. Funct. Mater.*, 2020, **30**, 1904576.

43 S. Wang, S. Zhou, Y. Tong, Z. Song, H. Wang, Q. Tang, X. Zhao and Y. Liu, *Adv. Mater. Interfaces*, 2019, **6**, 1801984.

44 S. Schott, E. Gann, L. Thomsen, S. H. Jung, J. K. Lee, C. R. McNeill and H. Sirringhaus, *Adv. Mater.*, 2015, **27**, 7356–7364.

45 A. F. Stassen, R. W. I. De Boer, N. N. Losad and A. F. Morpurgo, *Appl. Phys. Lett.*, 2004, **85**, 3899–3901.

46 H. Zajaczkowska, L. Veith, W. Waliszewski, M. A. Bartkiewicz, M. Borkowski, P. Sleczkowski, J. Ulanski, B. Graczykowski, P. W. M. Blom, W. Pisula and T. Marszalek, *ACS Appl. Mater. Interfaces*, 2021, **13**, 59012–59022.

47 G. Giri, S. Park, M. Vosgueritchian, M. M. Shulaker and Z. Bao, *Adv. Mater.*, 2014, **26**, 487–493.

48 S. Choi, C. Fuentes-Hernandez, C. Y. Wang, T. M. Khan, F. A. Larrain, Y. Zhang, S. Barlow, S. R. Marder and B. Kippelen, *ACS Appl. Mater. Interfaces*, 2016, **8**, 24744–24752.

49 Y. Ito, A. A. Virkar, S. Mannsfeld, J. Hak Oh, M. Toney, J. Locklin, Z. Bao, A. A. Virkar, S. Mannsfeld, H. O. Joon, M. Toney, J. Locklin and Z. Bao, *J. Am. Chem. Soc.*, 2009, **131**,

9396–9404.

50 M. J. Frisch, G. W. Trucks, H. B. Schlegel, G. E. Scuseria, M. A. Robb, J. R. Cheeseman, G. Scalmani, V. Barone, G. A. Petersson and H. Nakatsuji, *Wallingford CT*.

51 E. F. Valeev, V. Coropceanu, D. A. da Silva Filho, S. Salman and J.-L. Brédas, *J. Am. Chem. Soc.*, 2006, **128**, 9882–9886.

52 J. P. Perdew, K. Burke and M. Ernzerhof, *Phys. Rev. Lett.*, 1996, **77**, 3865.

53 M. M. Francl, W. J. Pietro, W. J. Hehre, J. S. Binkley, M. S. Gordon, D. J. DeFrees and J. A. Pople, *J. Chem. Phys.*, 1982, **77**, 3654–3665.

54 Q. Ai, V. Bhat, S. M. Ryno, K. Jarolimek, P. Sornberger, A. Smith, M. M. Haley, J. E. Anthony and C. Risko, *J. Chem. Phys.*, 2021, **154**, 174705.

55 S. F. Nelsen, S. C. Blackstock and Y. Kim, *J. Am. Chem. Soc.*, 1987, **109**, 677–682.

56 R. Baer, E. Livshits and U. Salzner, *Annu. Rev. Phys. Chem.*, 2010, **61**, 85–109.

57 T. M. Henderson, A. F. Izmaylov, G. Scalmani and G. E. Scuseria, *J. Chem. Phys.*, 2009, **131**, 44108.

58 F. Weigend and R. Ahlrichs, *Phys. Chem. Chem. Phys.*, 2005, **7**, 3297–3305.

59 S. Wen, A. Li, J. Song, W. Deng, K. Han and W. A. Goddard, *J. Phys. Chem. B*, 2009, **113**, 8813–8819.

60 R. A. Marcus, *Annu. Rev. Phys. Chem.*, 1964, **15**, 155–196.